Long-range plasmonic directional coupler switches controlled by nematic liquid crystals

D. C. Zografopoulos* **and R. Beccherelli**

Consiglio Nazionale delle Ricerche, Istituto per la Microelettronica e Microsistemi (CNR-IMM), Roma 00133, Italy

*dimitrios.zografopoulos@artov.imm.cnr.it

Abstract: A liquid-crystal tunable plasmonic optical switch based on a long-range metal stripe directional coupler is proposed and theoretically investigated. Extensive electro-optic tuning of the coupler's characteristics is demonstrated by introducing a nematic liquid crystal layer above two coplanar plasmonic waveguides. The switching properties of the proposed plasmonic structure are investigated through rigorous liquid-crystal studies coupled with a finite-element based analysis of light propagation. A directional coupler optical switch is demonstrated, which combines very low power consumption, low operation voltages, adjustable crosstalk and coupling lengths, along with sufficiently reduced insertion losses.

OCIS codes: (130.3120) Integrated optics devices; (130.4815) Optical switching devices; (230.3720) Liquid-crystal devices; (240.6680) Surface plasmons; (200.4650) Optical interconnects.

References and links

1. T. W. Ebbesen, C. Genet, and S. I. Bozhevolnyi, "Surface-plasmon circuitry," Phys. Today **61**, 44–50 (2008).
2. M. I. Stockman, "Nanoplasmonics: past, present, and glimpse into future," Opt. Express **19**, 22029–22106 (2011).
3. E. Le Ru and P. Etchegoin, *Principles of Surface Enhanced Raman Spectroscopy and Related Plasmonic Effects* (Elsevier, Amsterdam, 2009).
4. D. K. Gramotnev and S. I. Bozhevolnyi, "Plasmonics beyond the diffraction limit," Nat. Photonics **4**, 83–91 (2010).
5. N. Pleros, E. E. Kriezis, and K. Vyrsokinos, "Optical interconnects using plasmonics and Si-photonics," IEEE Photon. J. **3**, 296–301 (2011).
6. S. Papaioannou, K. Vyrsokinos, O. Tsilipakos, A. Pitilakis, K. Hassan, J.-C. Weeber, L. Markey, A. Dereux, S. I. Bozhevolnyi, A. Miliou, E. E. Kriezis, and N. Pleros, "A 320 Gb/s-throughput capable 2x2 silicon-plasmonic router architecture for optical interconnects," J. Lightwave Technol. **29**, 3185–3195 (2011).
7. O. Tsilipakos, A. Pitilakis, T. V. Yioultsis, S. Papaioannou, K. Vyrsokinos, D. Kalavrouziotis, G. Giannoulis, D. Apostolopoulos, H. Avramopoulos, T. Tekin, M. Baus, M. Karl, K. Hassan, J.-C. Weeber, L. Markey, A. Dereux, A. Kumar, S. I. Bozhevolnyi, N. Pleros, and E. E. Kriezis, "Interfacing dielectric-loaded plasmonic and silicon photonic waveguides: Theoretical analysis and experimental demonstration," IEEE J. Quantum Electron. **48**, 678–687 (2012).
8. S. Papaioannou, D. Kalavrouziotis, K. Vyrsokinos, J.-C. Weeber, K. Hassan, L. Markey, A. Dereux, A. Kumar, S. I. Bozhevolnyi, M. Baus, T. Tekin, D. Apostolopoulos, H. Avramopoulos, and N. Pleros, "Active plasmonics in WDM traffic switching applications," Sci. Rep. **2**, 652 (2012).
9. J. J. Ju, S. Park, M.-S. Kim, J. T. Kim, S. K. Park, Y. J. Park, and M.-H. Lee, "40 Gbits/s light signal transmission in long-range surface plasmon waveguides," Appl. Phys. Lett. **91**, 171117 (2007).
10. S. Park, J. J. Ju, J. T. Kim, M.-S. Kim, S. K. Park, J.-M. Lee, W.-J. Lee, and M.-H. Lee, "Sub-dB/cm propagation loss in silver stripe waveguides," Opt. Express **17**, 697–702 (2009).
11. J. J. Ju, S. Park, M.-S. Kim, J. T. Kim, S. K. Park, Y. J. Park, and M.-H. Lee, "Polymer-based long-range surface plasmon polariton waveguides for 10-Gbps optical signal transmission applications," J. Lightwave Technol. **26**, 1510–1518 (2008).

#182210 - $15.00 USD Received 27 Dec 2012; revised 26 Feb 2013; accepted 3 Mar 2013; published 28 Mar 2013

12. J. T. Kim, J. J. Ju, S. Park, M.-S. Kim, S. K. Park, and M.-H. Lee, "Chip-to-chip optical interconnect using gold long-range surface plasmon polariton waveguides," Opt. Express **16**, 13133–13138 (2008).
13. P. Berini, "Long-range surface plasmon polaritons," Adv. Opt. Photon. **1**, 484–588 (2009).
14. T. Nikolajsen, K. Leosson, and S. I. Bozhevolnyi, "Surface plasmon polariton based modulators and switches operating at telecom wavelengths," Appl. Phys. Lett. **85**, 5833–5835 (2004).
15. A. Boltasseva and S. I. Bozhevolnyi, "Directional couplers using long-range surface plasmon polariton waveguides," IEEE J. Sel. Top. Quant. Electron. **12**, 1233–1241 (2006).
16. R. Charbonneau, C. Scales, I. Breukelaar, S. Fafard, N. Lahoud, G. Mattiussi, and P. Berrini, "Passive integrated optics elements based on long-range surface plasmon polaritons," J. Lightwave Technol. **24**, 477–494 (2006).
17. G. Gagnon, N. Lahoud, G. A. Mattiussi, and P. Berrini, "Thermally activated variable attenuation of long-range surface plasmon-polariton waves," J. Lightwave Technol. **24**, 4391–4402 (2006).
18. D. C. Zografopoulos, R. Asquini, E. E. Kriezis, A. d'Alessandro, and R. Beccherelli, "Guided-wave liquid-crystal photonics," Lab Chip **12**, 3598–3610 (2012).
19. I. Abdulhalim, "Optimized guided mode resonant structure as thermooptic sensor and liquid crystal tunable filter," Chin. Opt. Lett. **7**, 667–670 (2009).
20. I. Abdulhalim, "Liquid crystal active nanophotonics and plasmonics: from science to devices," J. Nanophotonics **6**, 061001 (2012).
21. P. A. Kossyrev, A. Yin, S. G. Cloutier, D. A. Cardimona, D. Huang, P. M. Alsing, and J. M. Xu, "Electric field tuning of plasmonic response of nanodot array in liquid crystal matrix," Nano Lett. **5**, 1978–1981 (2005).
22. Y. J. Liu, Q. Hao, J. S. T. Smalley, J. Liou, I. C. Khoo, and T. J. Huang, "A frequency-addressed plasmonic switch based on dual-frequency liquid crystals," Appl. Phys. Lett. **97**, 091101 (2010).
23. L. De Sio, R. Caputo, U. Cataldi, and C. Umeton, "Broad band tuning of the plasmonic resonance of gold nanoparticles hosted in self-organized soft materials," J. Mater. Chem **21**, 18967–18970 (2011).
24. L. De Sio, A. Cunningham, V. Verrina, C. M. Tone, R. Caputo, T. Bürgi, and C. Umeton, "Double active control of the plasmonic resonance of a gold nanoparticle array," Nanoscale **4**, 7619–7623 (2012).
25. A. C. Tasolamprou, D. C. Zografopoulos, and E. E. Kriezis, "Liquid crystal-based dielectric loaded surface plasmon polariton optical switches," J. Appl. Phys. **110**, 093102 (2011).
26. J. S. T. Smalley, Y. Zhao, A. A. Nawaz, Q. Hao, Y. Ma, I.-C. Khoo, and T. J. Huang, "High contrast modulation of plasmonic signals using nanoscale dual-frequency liquid crystals," Opt. Express **19**, 15265–15274 (2011).
27. A. E. Çetin, A. A. Yanik, A. Mertiri, S. Erramilli, Ö. E. Müstecaplıoğlu, and H. Altug, "Field-effect active plasmonics for ultracompact electro-optic switching," Appl. Phys. Lett. **101**, 121113 (2012).
28. D. C. Zografopoulos and R. Beccherelli, "Plasmonic variable optical attenuator based on liquid-crystal tunable stripe waveguides," Plasmonics (2013). DOI:10.1007/s11468-012-9440-7.
29. D. C. Zografopoulos, R. Beccherelli, A. C. Tasolamprou, and E. E. Kriezis, "Liquid-crystal tunable waveguides for integrated plasmonic components," Photon. Nanostruct.: Fundam. Appl. **11**, 73–84 (2013).
30. J. Pfeifle, L. Alloatti, W. Freude, J. Leuthold, and C. Koos, "Silicon-organic hybrid phase shifter based on a slot waveguide with a liquid-crystal cladding," Opt. Express **20**, 15359–15376 (2012).
31. A. d'Alessandro, B. Bellini, D. Donisi, R. Beccherelli, and R. Asquini, "Nematic liquid crystal optical channel waveguides on silicon," IEEE J. Quantum Electron. **42**, 1084–1090 (2006).
32. D. Donisi, B. Bellini, R. Beccherelli, R. Asquini, G. Gilardi, M. Trotta, and A. d'Alessandro, "A switchable liquid-crystal optical channel waveguide on silicon," IEEE J. Quantum Electron. **46**, 762–768 (2010).
33. A. K. Pitilakis, D. C. Zografopoulos, and E. E. Kriezis, "In-line polarization controller based on liquid-crystal photonic crystal fibers," J. Lightwave Technol. **29**, 2560–2569 (2011).
34. B. Bellini and R. Beccherelli, "Modelling, design and analysis of liquid crystal waveguides in preferentially etched silicon grooves," J. Phys. D: Appl. Phys. **42**, 045111 (2009).
35. J. F. Strömer, E. P. Raynes, and C. V. Brown, "Study of elastic constant ratios in nematic liquid crystals," Appl. Phys. Lett. **88**, 051915 (2006).
36. R. D. Schaller, L. F. Lee, J. C. Johnson, L. H. Haber, R. J. Saykally, J. Vieceli, I. Benjamin, T.-Q. Nguyen, and B. J. Schwartz, "The nature of interchain excitations in conjugated polymers: spatially-varying interfacial solvatochromism of annealed MEH-PPV films studied by near-field scanning optical microscopy (NSOM)," J. Phys. Chem. B **106**, 9496–9506 (2002).
37. J. Robertson, "High dielectric constant oxides," Eur. Phys. J. **28**, 265–291 (2004).
38. C. Vassallo, *Optical Waveguide Concepts* (Elsevier, Amsterdam, 1991).
39. Norland Products, Optical Adhesives, (www.norlandprod.com).
40. M. Wang, ed., *Lithography* (InTech, 2010).
41. CYCLOTENE, Dow Chemical, (www.dow.com).
42. J. Li, S.-T. Wu, S. Brugioni, R. Meucci, and S. Faetti, "Infrared refractive indices of liquid crystals," J. Appl. Phys. **97**, 073501 (2005).
43. B. Tatian, "Fitting refractive-index data with the Sellmeier dispersion formula," Appl. Opt. **23**, 4477–4485 (1984).
44. E. D. Palik, *Handbook of optical constants of solids* (Orlando, FL, Academic, 1985).
45. S. Laux, N. Kaiser, A. Zöller, R. Götzelmann, H. Lauth, and H. Bernitzki, "Room-temperature deposition of indium tin oxide thin films with plasma ion-assisted evaporation," Thin Solid Films **335**, 1–5 (1998).

#182210 - $15.00 USD Received 27 Dec 2012; revised 26 Feb 2013; accepted 3 Mar 2013; published 28 Mar 2013

46. T. Srivastava and A. Kumar, "Comparative study of directional couplers utilizing long-range surface plasmon polaritons," Appl. Optics **49**, 2397–2402 (2010).
47. A. Degiron, C. Dellagiacoma, J. G. McIlhargey, G. Shvets, O. J. F. Martin, and D. R. Smith, "Simulations of hybrid long-range plasmon modes with application to 90° bends," Opt. Lett. **32**, 2354–2356 (2007).
48. I. Abdulhalim, "Surface plasmon TE and TM waves at the anisotropic film-metal interface," J. Opt. A: Pure Appl. Opt. **11**, 015002 (2009).
49. R. Li, C. Cheng, F.-F. Ren, J. Chen, Y.-X. Fan, J. Ding, and H.-T. Wang, "Hybridized surface plasmon polaritons at an interface between a metal and a uniaxial crystal," Appl. Phys. Lett. **92**, 141115 (2008).
50. COMSOL Multiphysics v4.3a, (www.comsol.com).
51. M. Stallein, C. Kolleck, and G. Mrozynski, "Improved analysis of the coupling of optical waves into multimode waveguides using overlap integrals," in "PIERS 2005 Proceedings," (Hangzhou, China, 2005), pp. 464–468.
52. S.-T. Wu, "Absorption measurements of liquid crystals in the ultraviolet, visible, and infrared," J. Appl. Phys. **84**, 4462–4465 (1998).
53. I. W. Steward, *The Static and Dynamic Continuum Theory of Liquid Crystals* (Taylor & Francis, London, 2004).

1. Introduction

Plasmonics, the scientific field dealing with the properties of plasmons, i.e., oscillating optical fields of free electron gases present in metallic structures, has become one of the most active research topics in the last years. The exploitation of unique properties of plasmons, such as light localization beyond the diffraction limit, offers a broad spectrum of unprecedented capabilities, which has already led to the demonstration of numerous applications. These span over a broad range of disciplines, with nano-scaled integrated photonics platforms [1], nano-antennas, superlenses and ultrafast nanoplasmonics [2], as well as advanced chemical detection techniques like surface-enhanced Raman spectroscopy (SERS) [3], biomedical sensoristic and treatment techniques [4] and solar energy conversion being key, yet not exclusive, examples.

Focusing on the context of integrated photonics circuitry, plasmons manifest as localized light waves that propagate along metal/dielectric interfaces, termed as surface plasmon polaritons (SPPs). The manipulation and routing of such optical waves has allowed for the demonstration of numerous plasmonic waveguides of different light confinement scales, which constitute promising solutions in view of future integrated photonics platforms for broadband optical signal processing as both intra- [5–8] and inter-chip optical interconnects [9–12].

The latter, in particular, are based on plasmonic long-range waveguides consisting in thin metal stripes [13] that are characterized by single-mode low propagation losses, measured down to sub-dB/cm levels for thin silver stripes in telecom wavelength [10]. Furthermore, they offer excellent mode matching to single-mode fibers (SMFs) with coupling values down to 0.1 dB measured for gold stripes butt-coupled to polarization-maintaining SMFs [11]. Their fabrication involves standard planar processing techniques, such as lithographic definition, metal vapor deposition, and lift-off, thus eliminating the need for deep etching techniques frequently required in the case of dielectric stripe/rib waveguides. Moreover, they are compatible with flexible polymer claddings, providing very good mechanical stability, a prerequisite, for instance, in the design of flexible printed circuit boards. Finally, LRSPP plasmonic waveguides provide the capability of dynamically controlling the optical signal by directly addressing the metal waveguides. Based on such properties, a variety of devices has been thus far demonstrated, such as modulators and switches, relying on the thermo-optic control of the background polymer refractive index, which is controlled via current injection through the metal waveguide [14–17].

Instead of thermo-optically controlling the optical properties of photonic waveguides, an alternative route towards dynamically tunable photonic devices involves the use of nematic liquid crystals (NLCs), inherently anisotropic materials whose properties can be extensively controlled via the application of external fields. Already established in the design and fabrication of dielectric-based photonic guided-wave components [18] or sensors [19], NLCs are currently being explored also as a tuning mechanism of the properties of plasmonic structures [20], for

#182210 - $15.00 USD Received 27 Dec 2012; revised 26 Feb 2013; accepted 3 Mar 2013; published 28 Mar 2013

instance to dynamically control the localized plasmon resonances of metallic nanostructures, such as nanodot [21], nanodisk [22], or nanoparticle [23, 24] arrays. In such structures, the electro-optic control of the LC molecular orientation has been successfully employed to tune the plasmon resonances in the surface of metallic nanoparticles dispersed in LC or nanostructures patterned on thin metal films. As far as guided-wave plasmonics is concerned, in view of integrated photonic circuitry, functional LC-based plasmonic components, such as variable attenuators, phase-shifters, switches, and modulators have been theoretically demonstrated in a variety of waveguide platforms [25–29], by exploiting the electro-optical control of nematic LCs in order to tune the modal properties of surface-propagating light waves. Based on capacitive operation, LC-plasmonic devices are not only free from current injection issues, such as electromigration or thermal diffusion crosstalk, but, more importantly, they allow for extremely low-power consumption, which may reach several orders of magnitude lower than their thermo-optic counterparts, in the nW range [30].

In this work, we present the design and theoretical analysis of a plasmonic optical switch based on the electro-optic control of a NLC-enhanced directional coupler composed of two long-range Au stripe waveguides. By proper application of a control voltage, the optical properties of the two waveguides are tuned individually, allowing for switching between the two operation states of the coupler, cross and bar. The LC molecular orientation profiles are calculated by solving for the coupled elastic and electrostatic underlying problems. The voltage-dependent modal properties of the structure are investigated via the finite-element method and light propagation through the switch is modelled by expanding the excitation field in the eigenvector basis of the supported photonic modes. Low switching voltages are predicted, approximately 2 V, while other key properties of the switch, namely crosstalk, coupling length, and insertion losses, can be adjusted by proper selection of the structural parameters. The proposed components are envisaged as ultra-low power consumption light routing elements in integrated photonic platforms for optical inter-connects.

2. Liquid-crystal switching in side-coupled metal stripe plasmonic waveguides

The cross-section layout of the proposed plasmonic coupler switch is shown in Fig. 1(a). Two grounded Au stripes of dimensions $w \times t$ are embedded in a polymer background of total thickness $h_{\text{sub}} + h_{\text{buf}}$, where h_{sub} and h_{buf} are the thicknesses of the substrate and buffer layers, respectively. Above the buffer layer, a planar cell is infiltrated with a nematic liquid-crystalline material. A thin PMMA layer isolates the LC-layer from two ITO electrodes of width w placed directly above the Au stripes. The structure is backed by a low-index material, silica in this case. This configuration allows for the individual addressing of each plasmonic waveguide, by properly applying a voltage V_{LC} on either ITO electrode, and minimizes the required applied voltage, since this is directly applied between the waveguiding Au stripes and the control electrodes. The application of the control voltage reorientates the LC molecules mainly in the region above a single Au stripe and thus tunes its optical properties, as it will be shown in this study. The local LC molecular orientation is described by the unit vector of the nematic director **n**, which is defined via the tilt and twist angles, as in Fig. 1(b). The total length of the LC-cell, which also defines the interaction length, is L_C, as shown in the three-dimensional perspective of Fig. 1(c). Finally, the separation between the two Au stripes is equal to d_C.

The operational principle of the 2×2 optical switch is based on the voltage-controlled detuning of either one of the adjacent Au stripes. The LC and polymer materials are selected such that the polymer index n_p is higher than the ordinary index n_o of the nematic material. In the rest case ($V_{\text{LC}} = 0$), the LC is oriented along the $z-$axis of the structure by applying proper strong anchoring conditions via, e.g., rubbed alignment layers or photo-alignment techniques. Typically used alignment layers, such as Nylon-6, have thicknesses in the order of tens of nm

#182210 - $15.00 USD Received 27 Dec 2012; revised 26 Feb 2013; accepted 3 Mar 2013; published 28 Mar 2013

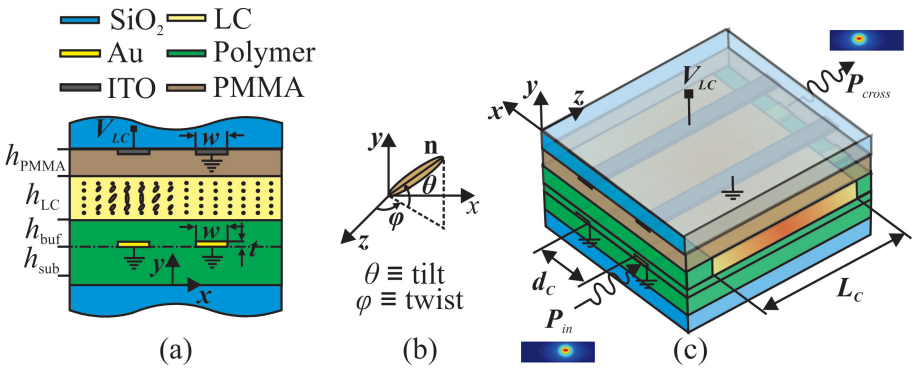

Fig. 1. (a) Cross-sectional view of the proposed LC-based plasmonic directional coupler and definition of material and structural parameters. Alignments layers (not shown) promote strong anchoring of the LC molecules along the $z-$axis at the LC/PMMA and LC/polymer interfaces. (b) Definition of tilt and twist angles that describe the nematic director local orientation. (c) Three-dimensional view of the proposed coupler. The coupling length is equal to L_C and the separation between the two metal stripes is d_C.

and optical properties similar to the polymers here used [31, 32]. It has been numerically verified that their presence has a negligible impact on the electrical and optical properties of the proposed coupler. TM-polarized light of the fundamental LRSPP mode launched in the input waveguide senses a low-index LC-layer ($n_o < n_p$) and remains confined in the polymer region, where it is coupled to the output port (cross-state) after a propagation distance $z = L_C$, as in typical LRSPP directional couplers. By applying a voltage in the cross ITO, the modal properties of the cross-waveguide are modified and for an optimum value $V_{\rm LC} = V_C$ the coupled optical power at $z = L_C$ is minimized (bar-state), as it will be demonstrated.

The rigorous study of LC reorientation when the control voltage is applied is a multiphysics problem, as it involves the elastic problem associated with LC deformations in the LC-layer bulk, inherently coupled to the electrostatic problem of the electric potential distribution in both LC and the surrounding dielectrics. This is achieved by solving for the set of three partial differential equations (PDEs) composed of two Euler-Lagrange equations that minimize the total energy stored in the LC region, along with Gauss' law, with independent variables the electric potential V and the tilt and twist angles. The PDEs are solved on the nodes of a finite-element mesh, that descritizes the cross-section of the structure, as described in detail in [29, 33]. An alternative approach involves the minimization of the total energy employing a weak formulation [34].

In this work the widely studied, commercially available, nematic mixture E7 is selected as the target LC material, characterized by low-frequency (measured at 1 KHz) dielectric constants perpendicular and parallel to the molecular director $\varepsilon_o = 5.3$ and $\varepsilon_e = 18.6$, respectively, and elastic constants K_{11}, K_{22}, K_{33} equal to 10.3, 7.4, and 16.48 pN, respectively [35]. The relative dielectric constants of the polymer, PMMA and SiO_2 are set to 4, 3.6 [36] and 3.9 [37], respectively. The LC and PMMA layers are correspondigly 5 μm and 1 μm thick, and the buffer and substrate thickness is, respectively, 2 μm and 10 μm. The ITO electrode's thickness is 100 nm and the Au stripe's dimensions are 5 μm × 15 nm.

Figure 2 shows the tilt and twist profiles in the LC layer plotted for $d_C = 3$ and 7 μm, as well as the potential distribution for the first case, when a 2 V voltage is applied at the cross ITO electrode. As both Au stripes and the bar ITO electrode are grounded, the electric field profile is highly asymmetric, with significant voltage drop only in the region of the cross waveguide,

#182210 - $15.00 USD Received 27 Dec 2012; revised 26 Feb 2013; accepted 3 Mar 2013; published 28 Mar 2013

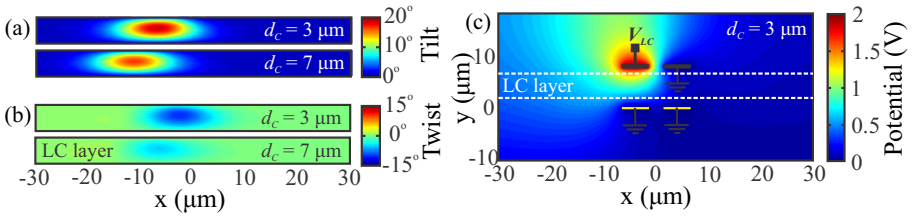

Fig. 2. (a) Tilt and (b) twist angle profile in the LC-layer for an applied voltage $V_{\mathrm{LC}} = 2$ V and a stripe separation equal to 3 and 7 μm. (c) Electric potential distribution plotted in the section between the silica substrates for $d_C = 3$ μm.

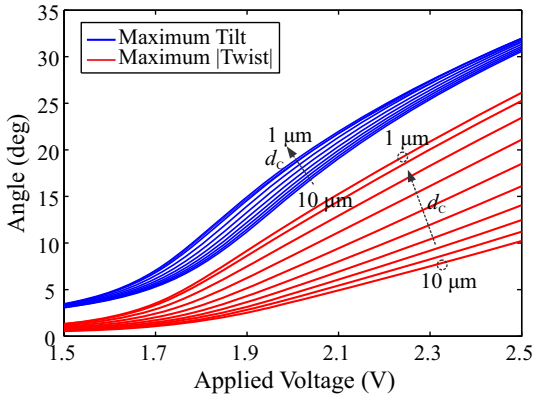

Fig. 3. Maximum tilt and twist angles in the voltage range between $V_{\mathrm{LC}} = 1.5$ and 2.5 V for a stripe separation from $d_C = 1$ to 10 μm. Shorter values of d_C lead to higher twist angles owing to stronger interaction of the electrostatic field with the grounded Au stripe and opposite ITO that define the bar port.

considering the gold stripe on the right as the reference input waveguide. On the contrary, both angles are practically zero above the bar port, which is placed between grounded Au and ITO stripes. When the two waveguides approach each other, the electrostatic field shows a stronger horizontal component, which leads to significantly higher values for the twist angles. This is observed in the results of Fig. 3, which shows the maximum tilt and twist values calculated for an applied voltage between 1.5 and 2.5 V, as a function of the stripe separation d_C. Calculations have been performed for a pretilt angle of 1°. It is demonstrated that twist is more sensitive than tilt to the variation of the distance d_C. Nevertheless, in terms of the electro-optic tuning of the structure's optical properties, it is the tilt angle that plays the most significant role, since it directly determines the effective refractive index along the $y-$axis, which is the one primarily sensed by TM-polarized light.

3. Optical properties of side-coupled metal stripe liquid-crystal plasmonic switches: CROSS state

In the absence of an applied voltage, the structure is symmetric with respect to the $x = 0$ plane, and the LRSPP mode senses a low index uniform LC overlayer. When launched in the input waveguide, optical power is progressively transferred to the cross port via evanascent coupling. Complete transfer is achieved after a propagation distance equal to the coupling length L_C, which can be calculated by the modal analysis of the coupler configuration. In particular, the structure supports two guided supermodes, characterized by symmetric (even) and anti-

#182210 - $15.00 USD Received 27 Dec 2012; revised 26 Feb 2013; accepted 3 Mar 2013; published 28 Mar 2013

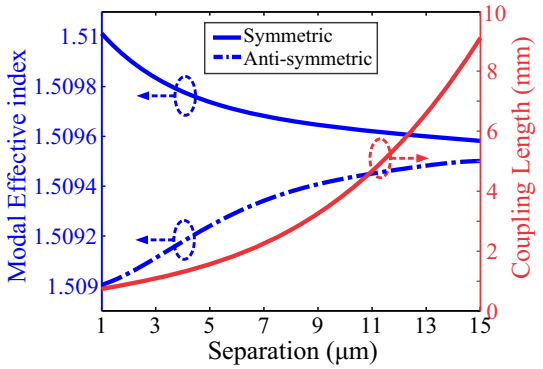

Fig. 4. Modal effective indices for the two TM-polarized supermodes supported of the coupler structure in the rest state ($V_{\mathrm{LC}} = 0$) as a function of the separation d_C, and corresponding coupling length L_C, defined as $L_C = 0.5\lambda_0/\Delta n$, where $\Delta n = n^{\mathrm{sym}} - n^{\mathrm{asym}}$, for $\lambda_0 = 1.55$ μm.

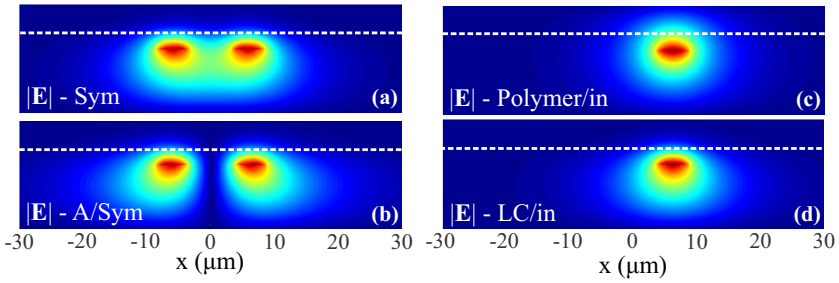

Fig. 5. Electric field modal profiles for the (a) symmetric and (b) anti-symmetric coupler supermodes for $d_C = 7$ μm and the (c) polymer and (d) LC-excitation modes.

symmetric (odd) profiles, respectively. At a given wavelength, the coupling length is given by $L_C = 0.5\lambda/\Delta n$, where $\Delta n = n^{\mathrm{sym}} - n^{\mathrm{asym}}$ the modal effective indices of the two supermodes [38]. In the proposed design, we opt for a polymer, such as the optical adhesive NOA-74 [39], characterized by $n_p = 1.51$ at the target wavelength of $\lambda_0 = 1.55$ μm [40]. Refractive indices of the other materials involved at λ_0 are equal to $n_{\mathrm{PMMA}} = 1.493$ [41], $n_o^{\mathrm{E7}} = 1.5024$, $n_e^{\mathrm{E7}} = 1.697$ [42], $n_{\mathrm{SiO_2}} = 1.444$ [43], $n_{\mathrm{Au}} = 0.5 - j11.5$ [44], and $n_{\mathrm{ITO}} = 1.27 - j0.12$ [45].

Figure 4 shows the modal indices of the two supermodes as a function of the separation d_C and the equivalent coupling lengths, which span in the millimeter range [46]. Figure 5(a-b) shows the supermodal electric field profiles calculated for $d_C = 7$ μm. The modal profiles demonstrate that the optical field is confined in the polymer region, as in LRSPP waveguide multilayer designs [47], without the optical field penetrating deep into the anisotropic LC layer. Unlike when metal films are directly in contact with an anisotropic dielectric material [48, 49], in the case under study the plasmonic modes retain the TM-polarization of typical LRSPP modes guided by thin metal stripes embedded in isotropic materials. The profile of the symmetric supermode indicates that the two waveguides are significantly coupled. Since this coupling is more intense as d_C decreases, the reduced coupling lengths of Fig. 4 are expected to be associated with moderate crosstalk values. In order to study the key optical properties of the coupler, apart from L_C, such as insertion losses and crosstalk, the eigenvalue expansion method is implemented. First, the tilt and twist angles derived by the LC-swithcing analysis, which determine the exact form of the optical dielectric tensor, are fed into a fully-anisotropic finite-element

#182210 - $15.00 USD Received 27 Dec 2012; revised 26 Feb 2013; accepted 3 Mar 2013; published 28 Mar 2013

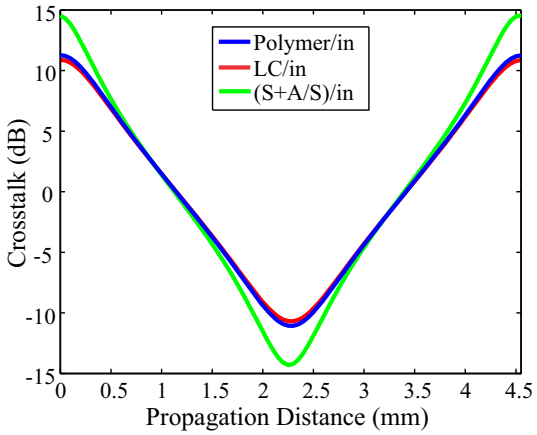

Fig. 6. Crosstalk evolution along a total propagation distance equal to $2L_C$ for three excitation scenarios: launching the polymer-input LRSPP mode (Fig. 5(a)), the LC-input LRSPP mode (Fig. 5(b)), or a superposition of the two coupler supermodes (Fig. 5(c-d)). The separation d_C is equal to 7 μm.

eigensolver [50], which yields the modal indices and field distributions of the supported supermodes with respect to the applied voltage V_{LC}. Subsequently, the switch is excited at one Au stripe by the equivalent single-waveguide LRSPP modes. Two excitation scenarios are considered, corresponding to the modal profiles shown in Fig. 5(c-d). In the first one, the excitation profile matches the LRSPP modes of a single Au stripe fully-embedded in polymer, i.e., in the absence of the LC layer, as schematically depicted in Fig. 1(c). The second scenario assumes excitation of the single-waveguide LRSPP mode of the LC-structure as in Fig. 1(a), calculated at the rest case.

The input excitation ($\mathbf{e}_i$) is then projected onto the set of the voltage-dependent eigenmodes ($\mathbf{e}_m$) and is expanded to this vector-basis. This allows for the calculation of the output field distribution ($\mathbf{e}_o$) at any propagation length according to the superposition of the analytically propagated eigenmodes

$$\mathbf{e}_o(x,y,z) = \sum_m \gamma_m \mathbf{e}_m(x,y) \exp(-jn_{\mathrm{eff}(m)} k_0 z), \tag{1}$$

where each eigenmode m is excited with a relative weight given by the complex-valued vector overlap integral [51]

$$\gamma_m = \frac{\iint_{A_\infty} \mathbf{e}_i \times \mathbf{h}_m^* \cdot \hat{\mathbf{z}}\, \mathrm{d}S}{\iint_{A_\infty} \mathbf{e}_m \times \mathbf{h}_m^* \cdot \hat{\mathbf{z}}\, \mathrm{d}S}. \tag{2}$$

Power transfer along the device for a given input is monitored by the output-port crosstalk XT, defined as the ratio of the guided-power $\mathrm{XT} = 10\log(P_B/P_C)$, where P_B, P_C is the percentage of optical power propagating in the semi-space defined by $x = 0$ and the bar and cross ports, respectively. Apart from the set of the two guided supermodes, radiation modes are also included in the eigenmode-expansion analysis given that, in general, the input fields are not linear superpositions of the guided supermodes only. Figure 6 shows the crosstalk evolution along propagation for $d_C = 7$ μm and for the two excitation scenarios, namely polymer- and LC-input. A reference case is also included, corresponding to launching a $1:1$ superposition of the two supermodes of the coupler. In this case, a minimum crosstalk value of near -15 dB is found at a propagation distance $z = L_C = 2.275$ mm. Contrarily, crosstalk for the two realistic

#182210 - $15.00 USD Received 27 Dec 2012; revised 26 Feb 2013; accepted 3 Mar 2013; published 28 Mar 2013

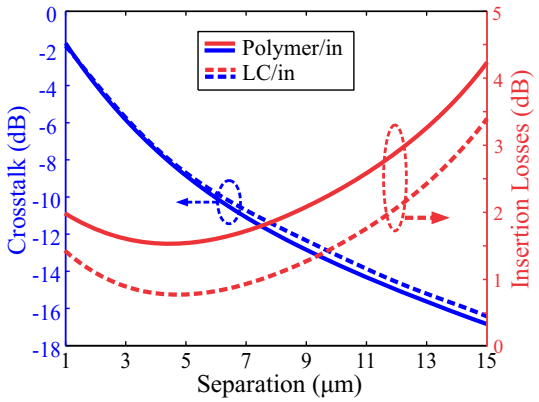

Fig. 7. Crosstalk values and insertion losses for the cross-state of the coupler as a function of stripe separation d_C for the two realistic excitation scenarios under study.

input scenarios is approximately -10 dB, since their modal profile does not excite equally the two supermodes, as it has been verified by the corresponding modal analysis.

Figure 7 investigates into the crosstalk and insertion losses of the switch, as a function of the separation d_C, asssuming a propagation length equal to the corresponding coupling lengths $L_C(d_C)$, as calculated in Fig. 4. Owing to close coupling between the two stripes, crosstalk for low values of d_C obtains very high values, up to -2 dB for $d_C = 1$ μm. It is thus verified that the reduction of the coupling length leads also to less efficient power transfer in terms of output crosstalk. The insertion losses are larger for the polymer-input case, as a part of the modal power is lost in the mismatch at the interface between polymer and LC-layer. However, for both input scenarios insertion losses are minimized at a separation of approximately 4.5 μm. Higher d_C values imply a longer component length and, subsequently, increased losses owing to dumping at the Au stripes. Structures with lower d_C values, although benefitting from reduced propagation losses, suffer from higher coupling losses at the input/output of the coupler, leading to overall higher insertion losses. Crosstalk values can be arbitrarily reduced, at the expense of larger component length, higher losses, and less dense integration of the adjacent waveguides. The selection of the optimal d_C value implies therefore a tradeoff between the target crosstalk and the acceptable losses and footprint of the switch. In the context of the present study, the value $d_C = 7$ μm, which provides a crosstalk lower than -10 dB is chosen in order to demonstrate the salient features of the switch's operation.

4. Optical properties of side-coupled metal stripe liquid-crystal plasmonic switches: BAR state

The analysis thus far focused in the rest case, which corresponds to the cross operation state of the switch. When the voltage V_{LC} is applied on a single stripe, as in Fig. 2, the structure is no longer symmetric, since a high-tilt zone is formed above the cross stripe waveguide, which translates in higher refractive index sensed by TM-polarized light. The modulation of the effective refractive index profile desynchronizes the coupled waveguides and progressively inhibits power coupling to the cross port. In our study, the optimal value $V_{\mathrm{LC}} = V_C$, which minimizes coupling at a length equal to L_C was found equal to 1.954 V. At this voltage value, the modal index difference for the LC-switched and the LC-off single Au stripe waveguide was found equal to $\Delta n = 5.979 \times 10^{-4}$, which deviates by $\sim 1.5\%$ with respect to the critical value predicted by the coupled mode theory given by $\Delta n_{\mathrm{cr}} = \sqrt{3}\lambda_0/2L_C$ [38]. Figure 8 shows

#182210 - $15.00 USD Received 27 Dec 2012; revised 26 Feb 2013; accepted 3 Mar 2013; published 28 Mar 2013

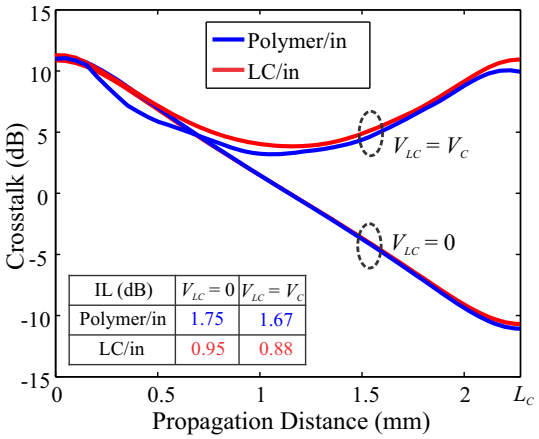

Fig. 8. Crosstalk evolution for the two excitation scenarios at $V_{\rm LC} = 0$ and $V_{\rm LC} = V_C = 1.954$ V, which correspond to operation in the CROSS and BAR state, respectively, for a propagation distance equal to the coupling length $L_C = 2.275$ mm. Inset shows the insertion losses of the component for both operation states and excitation profiles.

crosstalk evolution for a propagation distance equal to L_C for both excitation scenarios and both operation states. It is demonstrated that the crosstalk at the output of the switch is ± 10 dB for the bar and cross-states, respectively.

Figure 9 monitors optical power propagation at the plane 100 nm above the Au stripes, for the LC-input scenario studied in Fig. 8 at both operation states of the switch, clearly demonstrating maximum/minimum power transfer in the cross/bar-state of the switch. An isolation of ~ 10 dB is observed in both cases owing to the proximity of the two waveguides, as discussed in the context of the results shown in Fig. 7. The corresponding multimedia files show optical power coupling along the propagation, monitored at the cross-section of the coupler. In the cross state, power transfer takes place between the identical plasmonic waveguides, without entering into the low-index LC layer. On the contrary, in the bar state, the cross waveguide is desynchronized, forming a hybrid plasmonic/LC-dielectric guide, whose modal index detuning leads to minimal power coupling at a propagation distance equal to L_C.

The inset in Fig. 8 shows the insertion losses of the component, which are by 0.07 dB higher in the bar-state, owing to a slightly better coupling efficiency of the excitation modes to the guided supermodes of the coupler in the cross-state. In this analysis, the LC material was considered to be lossless. Absorption losses are likely below 1 dB/cm, as measured for the pure compound 5CB, one of the components of E7 [52]. In practice, however, LC photonic waveguiding structures exhibit scattering losses, which may range typically in the range from few [31, 32] to tens of dB/cm [30]. We have repeated the study of the coupler as in Fig. 8 by introducing different levels of losses via the imaginary part of the LC indices, such that the individual LC-waveguide formed in the switched LC-layer, i.e., in the absence of the plasmonic waveguides at $V = V_{\rm LC}$, exhibits propagation losses of 5 and 20 dB/cm. The insertion losses of the device were practically unaffected in all cases examined with reference to the cross-state, since the amount of optical power that enters the LC layer was found less than 3%. In the bar-state, a part of the propagating optical field enters in the high-index LC-zone formed under the control ITO electrode, as shown in the multimedia file associated with Fig. 9(b). In that case, the insertion losses for both excitation scenarios were found to increase by 0.1 and 0.7 dB, respectively, for the two levels of losses considered.

The switching speed of the device is expected in the millisecond range, as in typical nematic

#182210 - $15.00 USD Received 27 Dec 2012; revised 26 Feb 2013; accepted 3 Mar 2013; published 28 Mar 2013

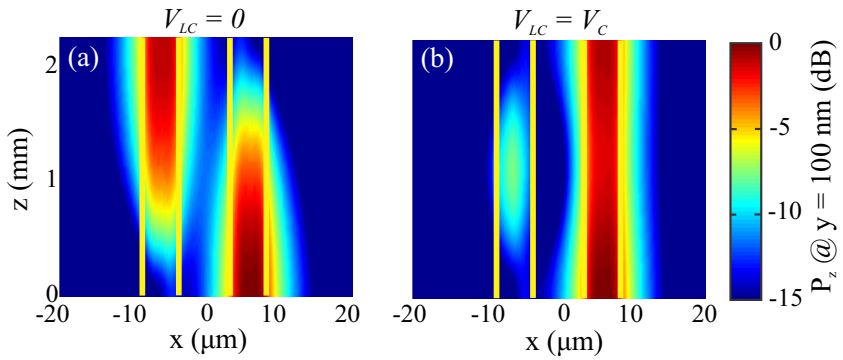

Fig. 9. Optical power propagation at 100 nm above the metal stripes for the (a) cross and (b) bar operation states calculated for the LC-excitation scenario, with parameters as in Fig. 8. The associated multimedia files monitor power coupling at the coupler's cross-section for the (a) cross (Media 1) and (b) bar (Media 2) state.

LC photonic components [53], which is sufficient for light reconfiguration and routing applications. The power consumption of the device can be estimated as $P \simeq C f V_{\mathrm{LC}}^2$, where C is the device capacitance and $f = 1 \div 10$ KHz the LC-switching frequency. By denoting as C^* the capacitance per unit length, an upper limit C^*_{max} could be given by considering the in-series capacitance combination of the three layers between the control electrodes, i.e., PMMA, LC, and polymer buffer. For relative permittivity and layer thickness values as in Section 2, this upper limit is approximately 40 pF/m. Assuming a device length of 2.5 mm, a driving voltage of 2 V, and a driving frequency of 1 KHz, the estimated power consumption is 0.4 nW, orders of magnitude lower than in thermo-optic plasmonic switching devices [8, 14, 17].

5. Conclusions

In brief, we have presented the design and analysis of a liquid-crystal long-range plasmonic directional coupler switch and investigated into its performance characteristics, namely coupling length, crosstalk and insertion losses. It has been demonstrated that coupling lengths in the few millimeter range allow for crosstalk values better than -10 dB with insertion losses lower than 2 dB and a switching voltage below 2 V. The material and structural parameters involved are compatible with standard fabrication processes, namely polymer spin-coating and metal patterning, deposition and lift-off, as demonstrated in numerous Au/polymer LRSPP fabricated components [13]. The LC-cell thickness and alignment techniques are also typical of planar cells infiltrated with nematic materials. These components are proposed as an ultra-low power solution, free from issues of their thermo-optic analogues, such as thermal crosstalk, diffusion and electromigration, in integrated photonic architectures for optical inter-chip interconnects.

Acknowledgments

This work was supported by the Marie-Curie Intra-European Fellowship ALLOPLASM (FP7-PEOPLE-2010-IEF-273528), within the 7th European Community Framework Programme.